5-11-2020

Nonlinear dynamic tests of a reinforced concrete frame building at different damage levels

Seyedsina Yousefianmoghadam

Mingming Song

Mohammad E. Mohammadi

Brittany Packard

Andreas Stavridis

See next page for additional authors

Authors

Seyedsina Yousefianmoghadam, Mingming Song, Mohammad E. Mohammadi, Brittany Packard, Andreas Stavridis, Babak Moaveni, and Richard L. Wood

Nonlinear dynamic tests of a reinforced concrete frame building at different damage levels

Seyedsina Yousefianmoghadam,[1] Mingming Song,[2] Mohammad Ebrahim Mohammadi,[3] Brittany Packard,[1] Andreas Stavridis,[1] Babak Moaveni,[2] Richard L. Wood[3]

1 Civil, Structural and Environmental Engineering, University at Buffalo, Buffalo, New York, USA

2 Civil and Environmental Engineering, Tufts University, Medford, Massachusetts, USA

3 Civil and Environmental Engineering, University of Nebraska-Lincoln, Lincoln, Nebraska, USA

Correspondence — Andreas Stavridis, Civil, Structural and Environmental Engineering, University at Buffalo, Buffalo, NY, USA. Email: astavrid@buffalo.edu

ORCIDs

Seyedsina Yousefianmoghadam https://orcid.org/0000-0001-7632-8561

Mingming Song https://orcid.org/0000-0002-1001-2326

Mohammad Ebrahim Mohammadi https://orcid.org/0000-0002-2368-3962

Andreas Stavridis https://orcid.org/0000-0001-9449-6796

Babak Moaveni https://orcid.org/0000-0002-8462-4608

Richard L. Wood https://orcid.org/0000-0002-8642-2217

Published in *Earthquake Engineering Structural Dynamics* **49** (2020), pp 924–945.
DOI: 10.1002/eqe.3271

Submitted 20 February 2019; revised 26 February 2020; accepted 28 February 2020; published 11 May 2020.
Suggested citation: Yousefianmoghadam S, Song M, Mohammadi ME, et al. Nonlinear dynamic tests of a reinforced concrete frame building at different damage levels. *Earthquake Engng Struct Dyn*. 2020;49:924–945. https://doi.org/10.1002/eqe.3271

Abstract
This paper discusses the dynamic tests of a two-story infilled reinforced concrete (RC) frame building using an eccentric-mass shaker. The building, located in El Centro, CA, was substantially damaged prior to the tests due to the seismic activity in the area. During the testing sequence, five infill walls were removed to introduce additional damage states and to investigate the changes in the dynamic properties and the nonlinear response of the building to the induced excitations. The accelerations and displacements of the structure under the forced and ambient vibrations were recorded through an array of sensors, while LIDAR scans were obtained to document the damage. The test data provide insight into the nonlinear response of an actual building and the change of its resonant frequencies and operational shapes due to varying damage levels and changes of the excitation amplitude, frequency, and orientation.

Keywords: dynamic testing, nonlinear response, reinforced concrete building, structural irregularities, system identification

1 Introduction

Reinforced concrete (RC) frame buildings with masonry infills are among the most commonly found structures in earthquake-prone areas around the world. Hence, a number of studies have experimentally and/or numerically investigated their seismic behavior. The majority of the experimental studies have focused on quasi-static tests of planar frames.[1–5] A few laboratory studies have included shake-table tests,[6–9] which provide insight into the dynamic behavior of these structures under cyclic loads at the component level. However, the specimens considered in these studies do not reflect the size and complexities of actual structures. Actual buildings have been instrumented to obtain their response to seismic excitations as part of the California Strong Motion Instrumentation Program (CSMIP) program,[10] and in rare cases tested.[11–13] However, in most cases, the excitations were not strong enough to push the structures into the nonlinear response range. Even in the few cases the buildings behaved nonlinearly, the data were obtained from a single state of damage. As a result, our understanding of the system-level nonlinear dynamic behavior of deteriorated buildings under dynamic loads, and of the effect of evolving damage, is incomplete. Moreover, the lack of varying levels of damage also prevents the assessment of the ability of system-identification methods to identify changes in the building dynamic properties due to damage in structural elements.

This paper describes the dynamic tests performed on a two-story RC building with masonry infills. The damage to the building due to the 2010 El Mayor Cucapah earthquake provided the opportunity to investigate the dynamic behavior of the structure. The tests involved the dynamic loading of the building using an eccentric-mass shaker, which pushed the structure into its nonlinear range of response. During the tests, infill walls on the perimeter bays were sequentially demolished, introducing four additional damage states. The dynamic tests allow the assessment of commonly used system-identification methodologies and provide insight into the effect of evolving damage on the dynamic properties of buildings. Furthermore, the test data are used to investigate the effect of excitation amplitude, frequency, and orientation on the nonlinear dynamic response of an actual building. Finally, LIDAR scans are used to quantify the evolution of damage on the RC columns and masonry infills.

2 Test structure

The two-story warehouse shown in **Figure 1** was built in the 1920s in El Centro, CA, and it was typical of the construction practice in California in that era. In plan, the building was 27.0 by 32.3 m (88.6 by 106.0

(a) View from northwest (b) View from southwest

(c) Second-story panoramic view

Figure 1 Test structure (prior to the tests)

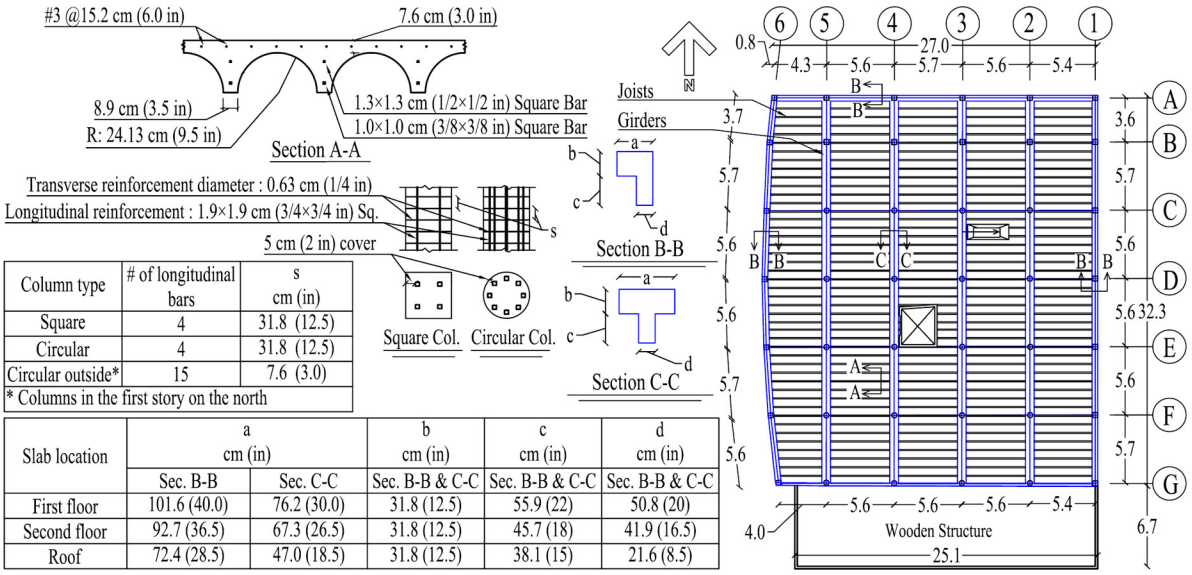

Column type	# of longitudinal bars	s cm (in)
Square	4	31.8 (12.5)
Circular	4	31.8 (12.5)
Circular outside*	15	7.6 (3.0)
* Columns in the first story on the north		

Slab location	a cm (in)		b cm (in)	c cm (in)	d cm (in)
	Sec. B-B	Sec. C-C	Sec. B-B & C-C	Sec. B-B & C-C	Sec. B-B & C-C
First floor	101.6 (40.0)	76.2 (30.0)	31.8 (12.5)	55.9 (22)	50.8 (20)
Second floor	92.7 (36.5)	67.3 (26.5)	31.8 (12.5)	45.7 (18)	41.9 (16.5)
Roof	72.4 (28.5)	47.0 (18.5)	31.8 (12.5)	38.1 (15)	21.6 (8.5)

Figure 2 Second-floor plan view and RC member detailing (units are in meters unless stated otherwise)

ft) as shown in **Figure 2**. The story height was 4.57 m (180 in), while the first-floor slab was 1.37 m (54 in) above the ground level, to allow for a basement, which had the same height as the stories above. The dimensions reported here are based on LIDAR data that indicate a small difference, up to 2%, in the bay lengths on the opposite ends (e.g., bay E-F/1 was 5.6 m [18.4 ft] long, whereas bay E-F/6 had a length of 5.7 m [18.7 ft]). The exterior infills on the northern side of the first story had a one bay recess to allow for a pedestrian sidewalk passage as shown in Figure 1a. On the south side, there was a one-story wooden structure attached to the building as shown in Figures 1b and 2. A 20.3-cm (8 in) thick RC parapet with an average height of 1.78 m (70 in) and an overall opening ratio of 23.4% was located at the roof.

The structural system included six-bay RC frames in the Y (north–south) direction connected by arch-type joists in the X (east–west) direction as shown in Figures 1c and 2. All interior columns and the columns on the south side of the building were circular with a diameter of 50.8 cm (20 in) in the basement and 40 cm (16 in) in the first and second floors. The exterior columns on the other three sides had square cross-sections of 40 by 40 cm (16 by 16 in). The dimensions and reinforcement details of the joists, girders, and columns are summarized in Figure 2. The structure sustained damage during the Imperial Valley earthquakes

Table 1 Characteristics of the major earthquakes experienced by the test structure

Event Name	Year	Magnitude	Depth, km (miles)	PGA (g)	Hypocenter distance from the building, km (miles)	Recording station distance from the building, km (miles)
Imperial Valley-02	1940	6.95	9 (6)	0.23	15.7 (9.8)	0.23 (0.14)
Imperial Valley-06	1979	6.53	10 (6)	0.22	33.6 (20.9)	1.26 (0.78)
Superstition Hills-02	1987	6.54	9 (6)	0.26	43.4 (27.0)	1.26 (0.78)
El Mayor Cucapah	2010	7.2	10 (6)	0.51	72.6 (45.1)	1.78 (1.11)

of 1940 and 1979, and the 1987 Superstition Hills earthquake. **Table 1**, which summarizes the characteristics of these earthquakes, indicates that peak ground acceleration (PGA) above 0.20 g was recorded within 1.8 km (1.1 miles) from the test structure. The building was repaired and retrofitted in the late 1980s, after the 1987 earthquake. The retrofit focused on strengthening the masonry infills along the exterior frames of the first story. As a result, there were three types of infill panels in this story: (a) the originally constructed double-wythe masonry infills that were not damaged nor retrofitted, (b) the infills of the first type retrofitted on both sides with concrete overlays reinforced with mesh reinforcement, and (c) RC infill panels constructed in the 1980s to replace the initially built masonry infills. The design details of the retrofitting scheme were not available, but it was most probably driven by the level of damage of each infill. The details of the infills in the first story, summarized in **Table 2**, indicate that the retrofitted infills, especially on the north frame, were significantly thicker and, therefore, considerably stiffer and stronger than the original infills. The exterior frames in the second story had masonry infills of two 10-cm (4 in) thick independent wythes, whereas the basement had RC walls along the building perimeter with openings near the top.

During the 2010 Baja El Mayor Cucapah earthquake, the structure was severely damaged and scheduled to be demolished after the completion of the tests as it could not be repaired cost-effectively. The damage concentrated in the second story infills and RC columns along the north, west, and south sides. Those along the east side of the second story and the entire first story did not develop any visible damage. **Figure 3** illustrates examples of observed damage that led to the evacuation of the building. The damage was quantified with LIDAR scans obtained before

Table 2 First story infills details

Infill location (see Figure 2)	Inside layer	Outside layer	Thickness		Rebar mesh spacing		Infills that are assumed to be the same
			Inside layer cm (in)	Outside layer cm (in)	Vertical cm (in)	Horizontal cm (in)	
B/4-5	Concrete	Masonry	30.5 (12)	20.3 (8)	N/M[a]	N/M[a]	B/1-2; B/2-3; B/3-4; B/5-6
B-C/6	Concrete	Concrete	19.0 (7.5)	0 (0)	47.0 (18.5)	46 (18)	
C-D/6	Masonry	Masonry	0 (0)	20.3 (8)	N/A[b]	N/A[b]	E-F/6
D-E/6	Concrete	Masonry	11.4 (4.5)	20.3 (8)	N/M[a]	N/M[a]	
F-G/6	Concrete	Concrete	19.0 (7.5)	0 (0)	49.0 (19.3)	43.9 (17.3)	
G/1-2	Concrete	Masonry	11.4 (4.5)	10.2 (4)	40.6 (16)	49.8 (19.6)	G/2-3; G/3-4; G/4-5;
G/5–6	Concrete	Masonry	11.4 (4.5)	10.2 (4)	40.6 (16)	50.8 (20)	
D-E/1	Plaster	Masonry	0.6 (0.25)	20.3 (8)	N/A[b]	N/A[b]	B-C/1; C-D/1; E-F/1
F-G/1	Concrete	Masonry	10.4 (4.1)	10.2 (4)	36.3 (14.3)	54.1 (21.3)	

a. Not measured due to time or access limitations.
b. Not applicable.

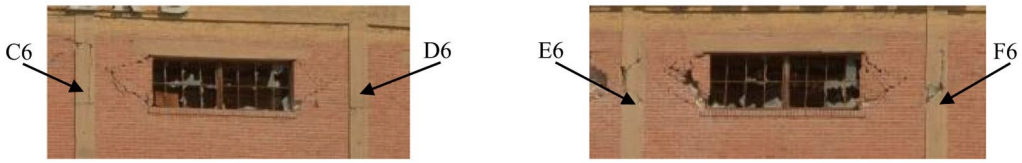

(a) Bay C-D/6 (see Figure 2) (b) Bay E-F/6 (see Figure 2)

Figure 3 Damage in the columns and masonry infills along the west side of the structure in the second story

and after the tests. These are discussed in detail in a following section. Due to the extensive damage, all nonstructural elements including the elevator and heating, ventilation, and air-conditioning (HVAC) were removed from the building prior to the tests and only the RC members and infills in the perimeter were in place during the tests.

2.1 Material properties

In situ and laboratory material tests were performed to obtain the mechanical and chemical properties of the masonry and RC elements. Concrete cores were extracted from the first-story slab, columns, and the retrofitted infill panel located in bay A/4-5. Masonry prisms were also extracted from the unretrofitted infills in the first and second stories.

Table 3 Mechanical material properties of concrete cylinders and masonry prisms

Structural Element	Number of samples	Density kg/m³ (pcf)	Core diameter cm (in)	Avg. modulus of elasticity GPa (ksi)	Avg. compressive strength MPa (psi)	Tensile strength MPa (psi)	Avg. strain at peak
Columns	2	2146.5 (134.0)	10.2 (4)	10.0 (1450)	19.9 (2890)	1.5 (217)	0.0034
Wall	1	N/A	10.2 (4)	7.4 (1073)	30.8 (4470)	N/A	0.0060
Slab	1	N/A 1	0.2 (4)	4.1 (590)	29.8 (4320)	3.5 (511)	0.0178
Masonry walls	2	1850.1 (115.5)	N/A	4.2 (611.5)	14.5 (2110)	N/A	0.0054

The cores and prisms were subjected to compression and split-cylinder tests in the Powell Laboratory at the University of California, San Diego. The test results, summarized in **Table 3**, indicate that the compressive strength of the concrete in the infills and slabs is within the range typically specified for modern construction. However, it is significantly lower in the columns. Furthermore, the modulus of elasticity for all of the concrete and masonry elements is lower than what current design codes such as ACI 318-14 and TMS 2016[14,15] estimate. The modulus of elasticity of the masonry infills was also estimated using an in situ test performed on an infill wall in the second story per ASTM C1197.[16] The modulus of elasticity estimated with this test was 3.5 GPa (513 ksi), that is, 16% lower than the average value obtained from the prism tests reported in Table 3. Samples of the longitudinal reinforcement extracted from RC beams and columns were tested in the Structural Engineering and Earthquake Simulation Laboratory at the University at Buffalo. The results, summarized in **Table 4**, indicate that the modulus of elasticity is similar to the currently used reinforcing bars. However, the yield and ultimate stresses are 283 and 421 MPa (41 and 61 ksi), respectively, indicating that Grade 40 steel was in this building.

Table 4 Mechanical properties of longitudinal steel bars

Cross section	Number of samples	Sectional area cm² (in²)	Modulus of elasticity GPa (ksi)		Yield stress MPa (ksi)		Ultimate strength MPa (ksi)		Strain at yield		Strain at failure[a]
			Mean	*SD*	Mean	*SD*	Mean	*SD*	Mean	*SD*	
Square	4	2.54 (0.39)	193 (28 000)	7.3 (1060)	281 (41)	15.4 (2.2)	421 (61)	16.5 (2.4)	0.0015	5.03e−5	0.245

a. Strain at failure was obtained from one sample due to instrumentation limitations.

Table 5 Masonry compressive test results

Test #	Location	Masonry height above test location cm (in)	Average compressive stress kPa (psi)
C1	G/3-4 (second story)	300 (118)	34 (5)
C2	E-F/1 (second story)	267 (105)	241 (35)
C3	G/3-4 (first story)	254 (100)	689 (100)

In situ compression tests were performed with flat jacks in accordance with ASTM C1196[17] to determine the dead load carried by the masonry infill walls. The results, summarized in **Table 5**, indicate that the vertical load carried by the infill on the south side of the second story, G/3-4, was significantly less than that carried by the infill on the east side of the same story (E-F/1). This difference can be justified by the direction of the slab joists, which transferred the loads along the X direction. Therefore, the infills along the east and west exterior frames carried more load than those along the north and south frames. In the first story, however, the load carried by the infill in the G/3-4 bay is considerably larger than that carried by the infill above it, despite the same joist arrangement in both floor slabs. This additional apparent load is probably caused by the concrete overlay, which engages this infill.

Shear tests at three different heights on a masonry infill in the second story were performed to estimate the shear strength of masonry bed joints with varying normal stress in accordance with ASTM C1531.[18] Based on the results summarized in **Table 6**, the angle of friction between the mortar and the bricks was 30_, and the cohesion was 143 kPa (20.8 Psi).

Table 6 Masonry shear test results

Test #	Location	Masonry height above test location cm (in)	Estimated gravity stress kPa (psi)	Masonry shear strength kPa (psi)
S1	E-F/1 (second story)	10 (4)	0 (0)[a]	152 (22)
S2	E-F/1 (second story)	257 (101)	186 (27)	221 (32)
S3	E-F/1 (second story)	345 (136)	255 (37)	310 (45)

a. Three bricks were removed above the location of test S1 to ensure that the bed joint does not carry gravity loads.

Table 7 Results of chemical analysis for mortar samples

Sample type	Sample #	Location	Sample mass g (oz)	Aggregate mass g (oz)	Soluble silica g (oz)	Volumetric ratio		
						Cement	CaCO	Aggregate
Mortar	M1	E-F/1 (second story)	10.00 (0.35)	7.03 (0.25)	0.14 (0.0049)	1	5	9
	M2	G/4-5 (first story)	10.00 (0.35)	7.36 (0.26)	0.14 (0.0049)	1	4	9
Plaster	P1	D-E/6 (first story)	10.00 (0.35)	7.85 (0.28)	0.12 (0.0042)	1	4	12
	P2	G/5-6 (first story)	10.00 (0.35)	8.01 (0.28)	0.12 (0.0042)	1	4	12

Chemical tests were also performed to estimate the binder/aggregate ratios and cement content in the various cementitious materials in the building. The method uses acid digestion and chemical analysis to identify soluble silica resulting from Portland cement hydration. The results, summarized in **Table 7**, indicate that only a small portion of the mortar and plaster binders consisted of Portland cement. The chemical analysis results of the concrete sampled from a column and a beam in the second story are summarized in **Table 8**. The aggregates to binder ratios are close to the range used for structural concrete used in modern construction.[19]

3 Induced damage

A preliminary computational model of the building was used to identify the walls with the highest impact on the dynamic properties of the structure. Based on this study and the limitations imposed by the building owner and the site access, five infill walls in the perimeter of the second story were removed at four stages during the testing sequence. The four levels of additional damage, referred to as damage states in this paper, were introduced to investigate the effect of evolving damage on the dynamic response, and to assess the ability of commonly used

Table 8 Results of acid digestion of concrete samples

Member	Location (second story)	Initial mass g (oz)	Binder mass g (oz.)	Aggregate mass g (oz)	Binder volume cm^3 (in^3)	Aggregate volume cm^3 (in^3)	Binder %	Aggregate %
Column	C/3	62.90 (2.22)	7.73 (0.27)	55.17 (1.95)	12.06 (0.74)	43.05 (2.63)	22	78
Beam	B-C/3-4	54.61 (1.93)	10.53 (0.37)	44.08 (1.55)	16.43 (1.00)	34.40 (2.10)	32	68

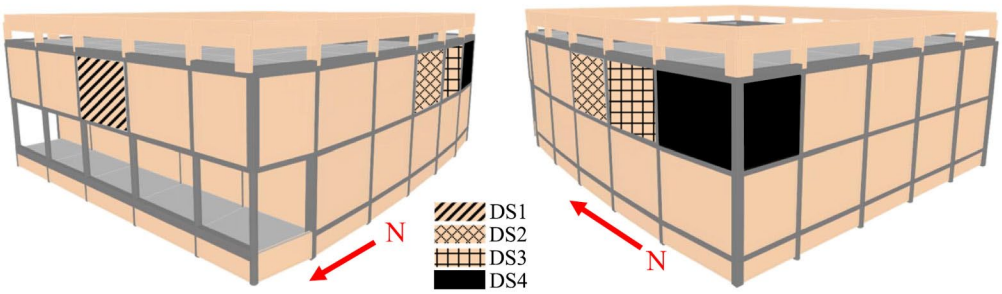

Figure 4 Damage states and wall removal sequence

system-identification techniques to capture the change of the dynamic properties. The initial damage state (DS0) was the result of the deterioration caused by aging and the earthquake sequence discussed in a previous section. Damage state DS1 was introduced by the removal of the infill in bay A/3-4 in the north side of the second story. This wall was removed prior to the tests to allow the insertion of the shaker inside the building. The second and third damage states (DS2 and DS3) were introduced by demolishing the infill walls in bays D-E/6 and E-F/6 in the west side of the second story, respectively. Finally, the fourth damage state (DS4) was introduced after the demolition of the infill panels in bays F-G/6 and G/5-6 in the second story, as shown in **Figure 4**.

4 Dynamic testing

4.1 Instrumentation

An array of 95 sensors including accelerometers and displacement sensors were installed in the building. To measure the acceleration, 60 force-balance accelerometers were installed close to the four corners and the center of the first- and second-floor slabs and the roof. In every location, the acceleration was measured in three directions (X, Y, and Z) for a total of 15 acceleration measurements at each level, as shown in **Figure 5**b. This instrumentation scheme was designed to record the translational and torsional response of the building. Moreover, two triaxial accelerometers were installed at the northwest and southeast corners of the basement, while three uniaxial accelerometers were mounted on the extension building at its north and west sides. These were installed

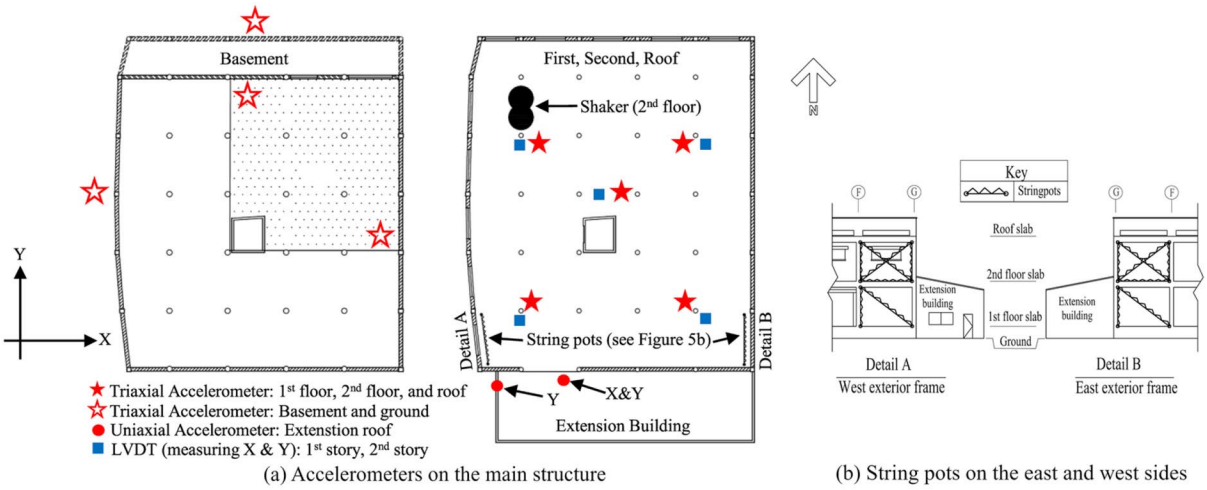

Figure 5 Instrumentation plan

to assess the unclear structural connection between the extension and main building through vibration propagation measurements. Finally, two triaxial accelerometers were placed on the ground close to the structure along the north and west sides to record any vibration of the soil due to waves generated by the interaction between the soil and the structure.

String pots and linear variable differential transformers (LVDTs) were used to measure the relative displacements between the floor slabs during the tests. The LVDTs were mounted at the top of poles installed near the accelerometers at the four corners and the center of the first and second floors, as shown in **Figure 6**. The poles were fixed on the lower

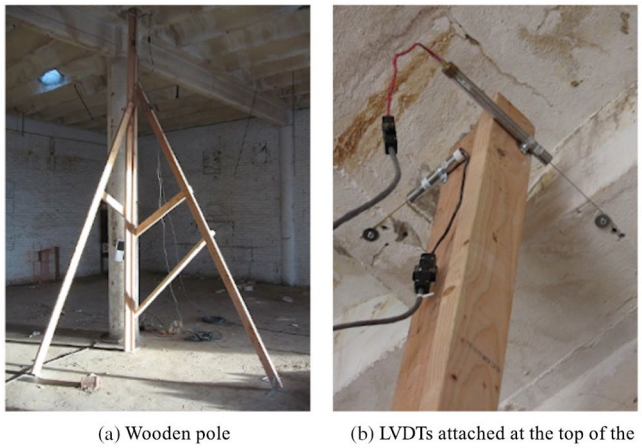

Figure 6 Poles used to mount LVDTs

slab and were 5 cm (2 in) short from the slab above so that the LVDTs installed at the top of the poles could measure the relative displacement of the two slabs in two horizontal directions (X and Y) at each location. The poles were designed to have low mass and high stiffness to ensure their vibration does not interfere with the measurement of the inter-story drift.[9] Their first-mode frequency was measured to be 12.3 Hz and can be filtered out from the recorded displacement time-histories as it is considerably higher than the vibration frequencies of the building. The string pots were installed at bays F-G/1 and F-G/6 in the first and second floor. They were oriented to measure the horizontal, vertical, and diagonal panel deformations as shown in Figure 5. The data sampling rate was 200 Hz, and all sensors were synchronized by GPS timing having an accuracy of less than 1 ms.[20]

4.2 Lidar data collection and processing methodology

The geometry of the structure, its components, and the damage are obtained through the processing of data collected with LIDAR scans before and after the test sequence as shown in **Figure 7**. The LIDAR survey consisted of 14 scans at DS0 and six scans at DS4 obtained from the locations indicated in Figure 7a. Due to time constraints, the posttest data collection was limited to the north and west sides where the majority of the test-induced damage was evidenced. Also, due to safety concerns, the roof was not scanned after the tests. The pretest scanning utilized a

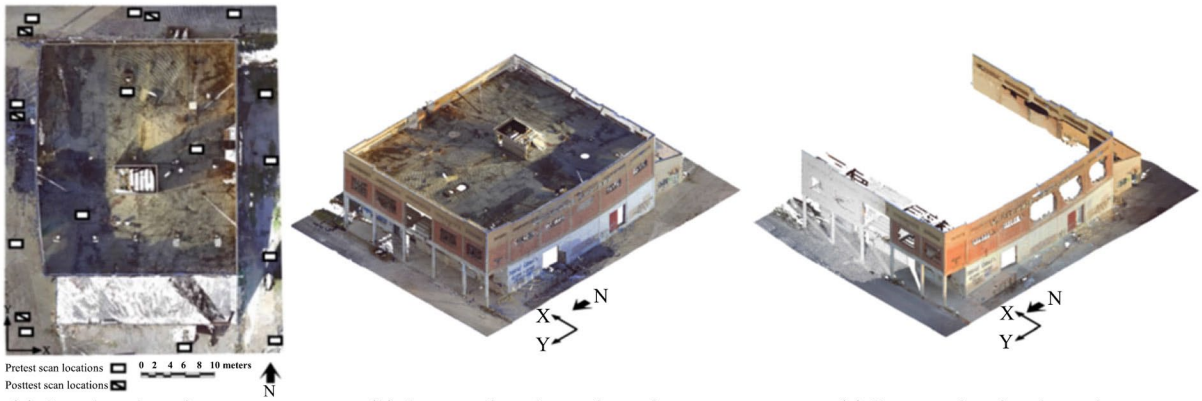

(a) Scan locations for pretest and posttest lidar setups

(b) Scan results prior to dynamic tests (pretest)

(c) Scan results after dynamic tests (posttest)

Figure 7 Lidar scan locations and isometric views of the registered point cloud sets

closed traverse strategy, as the last scan significantly overlapped with the first scan, to capture details of all exterior sides of the structure and minimize errors associated with the process of transforming and aligning two or more LIDAR scans to a unified coordinate system,[21] also known as registration. The scanner distance from the building was in all cases less than 10 m (33 ft), so that subcentimeter resolution could be maintained. Based on the selected scanner setting and the offset distances, the point-to-point spacing is at least 6 mm (0.24 in) for the pretest and posttest point clouds.

The registration process employed both paper checkerboard targets and additive manufactured retroreflective spheres. The cloud-to-cloud optimization, which matches the surfaces of objects and their features between two or more scans, was also performed to enhance the registration results. The mean registration error for the pretest point cloud was 1.50 mm (0.059 in). The posttest LIDAR scans were aligned to the pretest point cloud to form a uniform coordinate system. As a result, a holistic scene of the test structure was created for visualization and geometry measurements. However, to facilitate the computation of test-induced displacements and interstory drift objectively, and to eliminate the registration error propagation, the posttest scans of each corner were also independently registered to the pretest conditions using the cloud-to-cloud optimization of nontransient features not located within the test structure (e.g., the sidewalk section). The mean registration errors of pretest to posttest scans for the northeast, northwest, and southwest corners are 0.75 (0.03 in), 1.27 (0.05 in), and 1.39 mm (0.05 in), respectively, indicating high accuracy in the registration process. The registration error is not provided for the southeast corner as posttest scans were not obtained at that corner due to access limitations.

To obtain the deformation profiles at the corners of the building, vertical slices segmented into 1-cm (0.4 in) bins are obtained at a small offset distance of approximately 8 to 10 cm (3 to 4 in) from the corner edges to minimize the noise induced by the scatter of the laser beam at the free edges. Each vertical bin is represented by the median point at its centroidal elevation. The 1-cm (0.4 in)-spaced points are filtered using the Hampel identifier to detect and remove any remaining outliers based on local statistical parameters of the neighboring points. A low-pass finite impulse response (FIR) filter of order 48 and a cutoff frequency of

1 Hz is used to remove surface roughness and create salient deformation profiles. For each point in the profile identified as sample x, the median and standard deviation of the sample's neighboring points (X_n) are computed. Then, the logical expression stated in Equation 1 is checked to detect the outliers:

$$|x - \text{median}|X_n|| Z_{1-\alpha/2} \times \sigma_n \tag{1}$$

where $Z_{1-\alpha/2}$ is a reference normal distribution and α is the significance level. When the above statement is true, an outlier is detected and the sample is replaced by the median value of its neighborhood.[22] In this study, considering four neighboring points, that is, a vertical dimension of 4 cm (1.6 in), and a significance level of 0.2, results in the most accurate noise elimination.

4.3 Testing method and sequence

A series of dynamic tests were performed on the structure to investigate its dynamic properties in the quasilinear and nonlinear ranges. The experiments were conducted using the eccentric-mass shaker shown in **Figure 8**a, which at the time of testing was owned and operated by NEES@UCLA. The shaker was bolted to the concrete slab on the second floor near the northwest corner. The location of the shaker was chosen to increase the torsional response and to introduce a more challenging case for the numerical models that are developed to simulate the response of the structure.[23] The shaker consisted of two circular shafts that could rotate with the same frequency, but an adjustable phase, to produce harmonic excitations in the direction of interest. The excitations

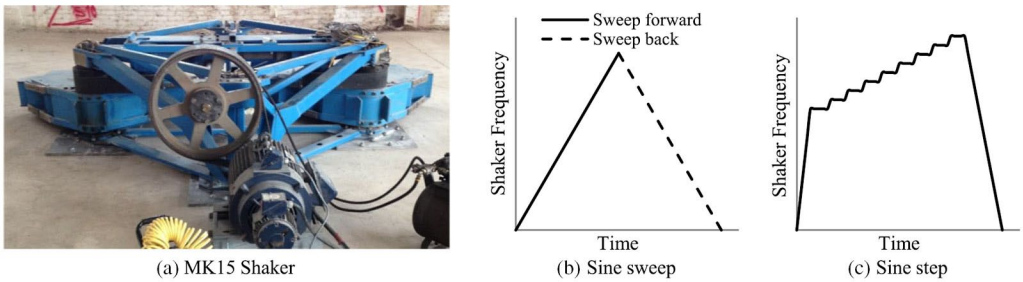

(a) MK15 Shaker (b) Sine sweep (c) Sine step

Figure 8 Shaker device and its forcing frequency scheme

produced by the shaker were sine sweeps and sine steps shown in Figures 8b and c, respectively. The inertia force induced on the building by the shaker can be estimated from Equation 2.

$$F = 2MR(2\pi f)^2 \tag{2}$$

where f is the forcing frequency of the shaker in Hz and MR is the product of the rotating mass and the distance between the center of rotation and the centroid of the mass inside each shaft. The maximum force the shaker could generate was 444.8 KN (100 kips). Hence, the weights inside each shaft could be adjusted depending on the desired range of excitation frequencies. In the tests, two mass setups were used: 193.57 kg-m (43.52 lb-in) and 652.38 kg-m (146.65 lb-in). The first setup could operate in the frequency range of 0–5.5 Hz, while the second setup could operate between 0 and 3 Hz. In this paper, the former setup is referred to as small mass (SM) and the latter setup as large mass (LM).

A total of 26 forced-vibration tests were conducted in DS1 through DS4 according to the testing protocol summarized in **Table 9**. No dynamic test was conducted in DS0 as the first wall had to be removed

Table 9 Summary of the test protocol

Test type	Excitation type	Damage state	Total # of tests	Excitation frequency range in Hz (# of tests in excitation direction) [shaker mass setup]
Forced vibration	Sine sweep	DS1	6	0.0–2.5 (2 in X, 1 in Y) [LM]; 0.0–3.0 (1 in X) [LM]; 0.0– 4.0 (1 in X, 1 in Y) [SM]
		DS2	3	0.0–3.0 (1 in X, 1 in Y) [LM]; 0.0–4.5 (1 in Y) [SM]
		DS3	1	0.0–4.5 (1 in Y) [SM]
		DS4	5	0.0–4.5 (1 in X, 1 in Y) [SM]; 0.0–5.5 (2 in X, 1 in Y) [SM]
	Sine step	DS1	5	1.3–2.5 (1 in X, 1 in Y) [LM]; 2.8–3.4 (1 in Y) [SM]; 3.5– 4.01 (1 in X, 1 in Y) [SM]
		DS2	3	1.3–2.3 (1 in X, 1 in Y) [LM]; 1.3–2.3 (1 in Y) [SM]
		DS3	1	1.3–2.3 (1 in Y) [SM]
		DS4	2	1.3–2.3 (1 in X, 1 in Y) [SM]
Ambient vibration	N/A	DS0	77	N/A
		DS1	379	
		DS2	20	
		DS3	6	
		DS4	19	

Abbreviations: LM, large mass; SM, small mass.

for the shaker to be moved inside the building. During the testing period, which lasted 5 days, the data acquisition system was continuously recording. Therefore, 120 hours of ambient vibrations of the structure were also recorded besides the forced vibrations.

5 System identification

The modal properties of the test structure are estimated at all damage states from the ambient- and forced-vibration data using the frequency-domain peak-picking method and the time-domain NExT-ERA method as discussed below.

5.1 Peak-picking method

The transfer functions between all accelerometer recordings, considered as outputs, and the recordings from a reference accelerometer, considered as the input, are computed to estimate the natural frequencies and mode shapes of the building. The accelerometers closest to the shaker, at the northwest corner of the second floor measuring either along the X or Y direction, depending on the direction of excitation, are selected as a reference for both the ambient- and the forced-vibration recordings to maintain consistency. The ambient-vibration recordings are split into 10- to 15-min segments resulting in 501 datasets, as summarized in Table 9. The recordings are then filtered using a FIR band-pass filter of order 1024 between 0.5 and 7 Hz. The power spectral densities (PSDs) are then estimated using the Welch method,[24] which is applied to the filtered data and averaged over 40-sec long Hanning windows with a 50% window overlap.[25] The frequencies corresponding to the peaks observed in the PSDs plots of the reference channels are considered as the modal frequencies. The mode-shape components are estimated using the values of the transfer functions at the corresponding estimated frequencies. The damping ratio of the structure is also estimated using the half-power bandwidth method from the transfer functions between the reference channels and the channels located above those at the roof level.

5.2 NExT-ERA method

The natural excitation technique combined with the eigensystem realization algorithm (NExT-ERA) is used to estimate the dynamic properties from the ambient-vibration recordings. NExT-ERA[26,27] is a time-domain method, which estimates the modal parameters of a system from its output measurements assuming that the input is a broadband white noise excitation. Although the ambient vibrations are not strictly white-noise excitations, NExT-ERA can provide accurate results even when the input excitation deviates from the ideal conditions.[28] In this study, the NExT-ERA algorithm is applied to 47 sets of ambient vibration data due to the computational effort required. This provides adequate data for the system identification and the comparison with the results from the frequency-domain method. For each set, the signal is divided into four Hamming windows with a 50% overlap to compute the cross-PSD functions between all channels and the reference accelerometer. The accelerometer measuring along the X-direction on the southwest corner of the roof is chosen here as the reference channel. The cross-correlation functions, which have the same form as the free vibration response of the building, are estimated as the inverse Fourier transform of the cross-PSD functions and are used as input to the ERA method. The order of ERA is chosen manually for each of the 47 sets based on the stabilization diagrams. The modal parameters, including the natural frequencies, damping ratios, and mode shapes are then estimated for each dataset.

5.3 System-identification results

The system identification results using ambient-vibration recordings, averaged over the available datasets at each damage state, are summarized in **Table 10**. There is a good agreement between the modal frequencies estimated using the NExT-ERA and the peak-picking methods with a maximum error of 4% for mode 1 at DS4. The mode shapes of the structure identified at DS1 for Modes 1 and 2 are illustrated in **Figure 9**. These mode shapes are 30-component unit vectors as they include five components for each orthogonal horizontal direction at the four corners and the center of the building at each floor level. The mode shapes shown in Figure 8 are obtained from the datasets yielding identified frequencies matching the average frequency values. The mode shapes

Table 10 Summary of system identification results

Damage state	Mode 1 frequency (Hz)			Mode 2 frequency (Hz)			Mode 1 damping ratio (%)						Mode 2 damping ratio (%)				MAC between NExT- ERA and peak picking			
	Peak picking		NExT-ERA	Peak Picking		NExT-ERA	Peak Picking (AV)	NExT-ERA	Peak picking (FV) Excitation direction				Peak picking (AV)	NExT-ERA	Peak picking (FV) Excitation direction[a]		Mode 1		Mode 2	
	AV	FV		AV	FV				X		Y				Y		AV	FV	AV	FV
									LM	SM	LM	SM			LM	SM				
DS1	2.24	1.73	2.26	3.32	2.19	3.37	1.7	1.5	6.5	-[a]	5.3	-[a]	3.1	2.5	8.3	-[a]	0.97	0.98	0.97	0.96
DS2	2.17	1.64	2.14	3.03	2.25	3.07	2.2	1.3	4.5	-[a]	3.4	5.5	2.1	2.6	7.8	5.3	1.00	1.00	1.00	0.99
DS3	2.12	1.61	2.06	3.00	2.17	2.96	2.4	1.9	-[a]	-[a]	-[a]	6.8	2.5	2.0	-[a]	5.4	1.00	0.96	1.00	0.98
DS4	2.05	1.61	1.96	2.81	2.15	2.72	1.4	1.6	-[a]	3.7	-[a]	4.3	2.5	2.8	-[a]	6.5	1.00	1.00	1.00	1.00

Abbreviations: AV, ambient vibration; FV, forced vibration; LM, large mass; SM, small mass.

a. Half band-width method could not estimate the damping ratios at that shaker setup and damage state (including the values for Mode 2 at all damage states for X excitations).

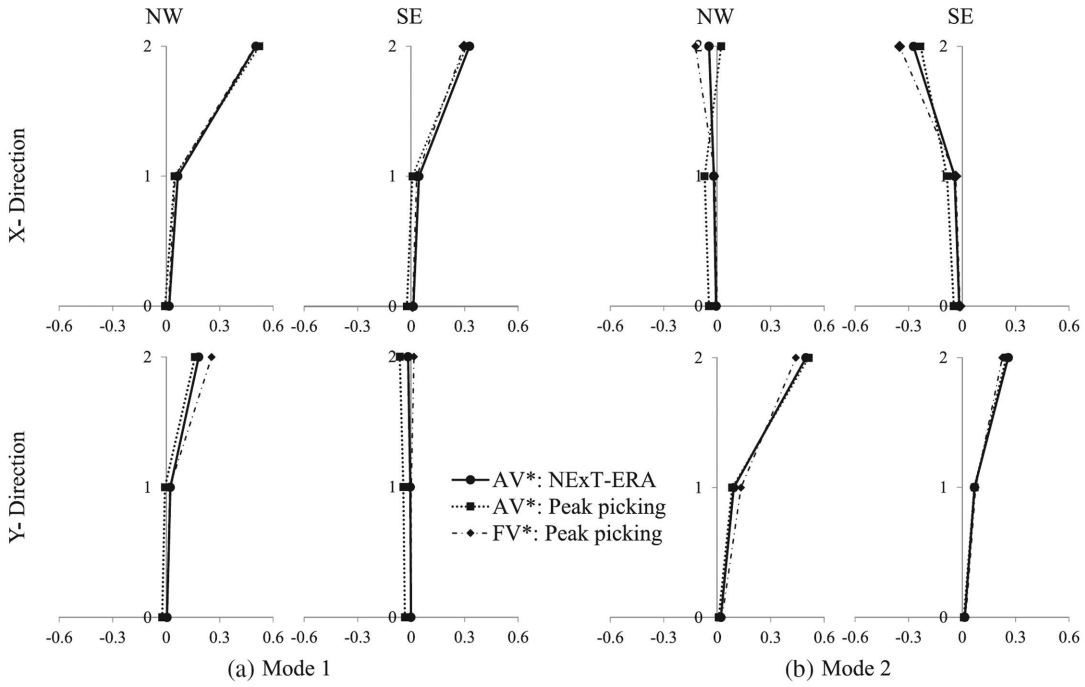

Figure 9 Identified shapes for Modes 1 and 2 at DS1. AV, ambient vibration; FV, forced vibration

estimated using the two system-identification methods indicate a good match as the Modal Assurance Criterion (MAC)[29] value is in all cases higher than 0.97, as shown in Table 10. This good agreement confirms the ability of the two methods to consistently estimate the modal frequencies and mode shapes.

The first mode mainly involves translation along X coupled with torsion as shown in Figures 9 and 10. The second mode combines translational along Y and torsion. The torsion can be attributed to the irregularities in the infills due to the openings and the nonuniform damage, which shift the center of rigidity towards the east side of the building.

Figure 9 also illustrates that the amplitude of the modal components corresponding to the first story is negligible compared with those estimated for the second story in both modes. This is attributed to the retrofit of the first story, which made it considerably stiffer than the second story. In fact, during the 2010 Baja California earthquake, the first story acted as a rigid block transferring the ground motion to the weaker second story. The extent and distribution of damage might have been different if both stories had been retrofitted and/or the structure had fewer irregularities.

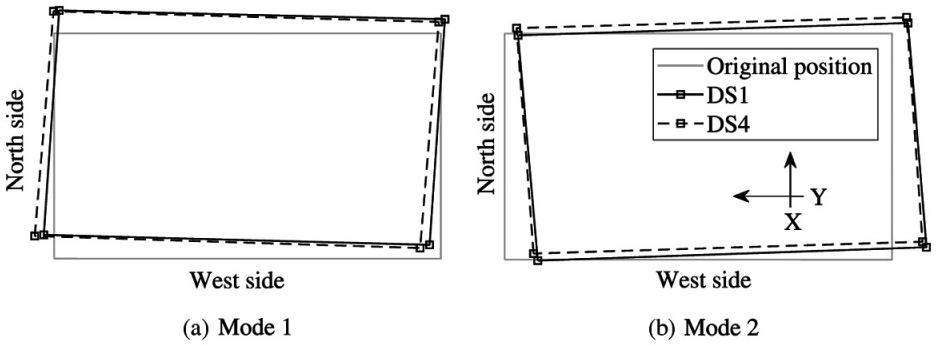

Figure 10 Deformed shape of the roof

The comparison of the mode shapes obtained in DS1 and DS4, shown in **Figure 10**, indicates that the change in the mode shapes due to the infill removal and the dynamic tests is not drastic. After the infill removal, the structure tended to sway on average 9.4% more in the Y direction for Mode 1 and 10.0% more in the X direction in Mode 2.

The identified frequencies for the first two modes during the 5 days of testing are shown in **Figure 11**. The modal frequencies identified from the ambient-vibration recordings decrease for both modes due to the damage induced by the removal of the infills. The drop varies for different damage states as the location of the removed infills and their prior level of damage affect their influence on the overall stiffness. The first infill was removed from bay A/3-4 along the north side (X direction) of the second story. Therefore, a drop in the frequency of Mode 1, which includes considerable translation in the X direction, is observed between DS0 and DS1. However, such drop is not evident in Mode 2, which involves translation mainly in the Y direction. The frequency drop between DS2 and DS3 is less than that between DS1 and DS2. The infills located in bays D-E/6 and E-F/6 were removed to introduce DS2 and DS3, respectively. The two infills had the same geometry but resulted in different frequency drops. The difference indicates that the E-F/6 infill had a smaller contribution to the lateral stiffness compared with the D-E/6 infill as it had sustained more damage during the 2010 earthquake.

A gradual decrease in the frequencies of both modes is also observed through each damage state, as shown in Figure 11, especially towards the end of DS1 and the following damage states. Because there was no element removal within the damage states, this decrease was caused by

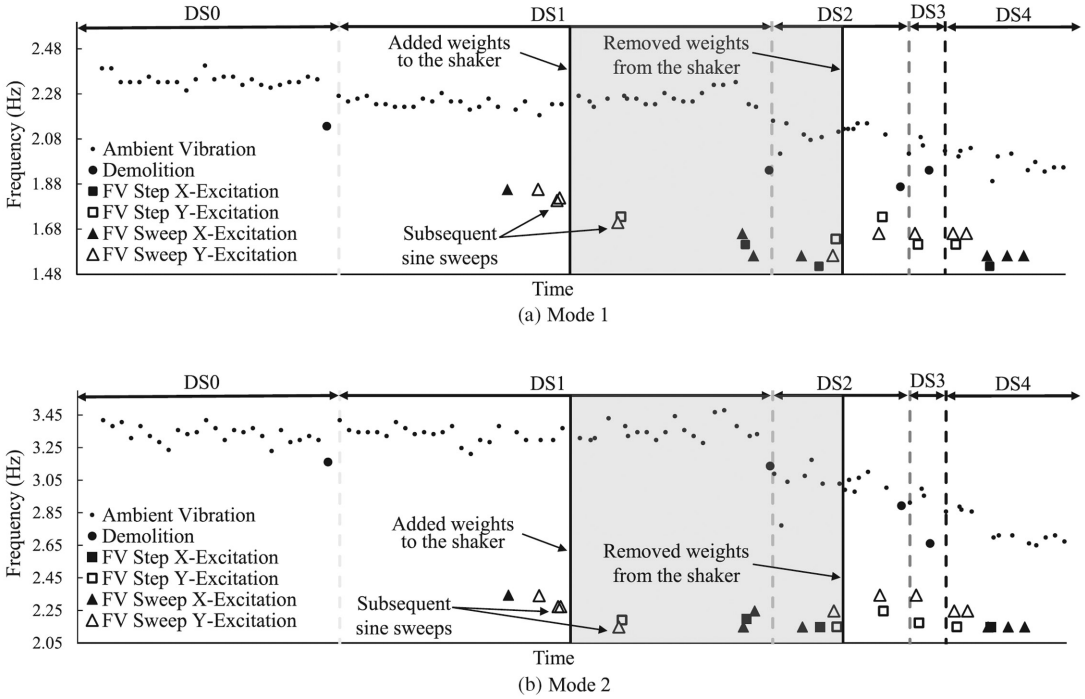

Figure 11 Identified natural frequency change of the structure during the testing period. FV, forced vibration

the damage introduced to the structure by the dynamic tests. The decrease is more evident during DS4 where the highest-amplitude forced vibrations were performed.

Table 10 also presents the damping ratios estimated from the ambient-vibration recordings. The small difference between the estimated values from the NExT-ERA and peak-picking methods can be expected considering the estimation uncertainty. Despite the scatter, the values are within 1.3%–2.4% of critical damping, with a mean value of 1.8%, for Mode 1 during the ambient vibrations. The estimated damping coefficient is slightly higher, between 2.0% and 3.1% with an average of 2.5%, for Mode 2. The damping values identified during the forced vibrations are significantly larger and reach almost 7% for Mode 1, and exceed 8% for Mode 2 for the tests with the large-mass setup. The effect of the amplitude of excitation on the damping ratio can also be noted by comparing the values estimated from two consecutive tests at DS2 with the only difference between the tests being the shaker mass. As indicated in Table 10, the damping ratios are higher in the tests conducted using the large-mass setup compared with the tests conducted with the

small-mass setup for both modes. The higher damping values are a result of the increased friction along the cracks in the masonry and concrete elements that get activated as the excitation level increases.

6 Forced-vibration test results

6.1 Transient response

6.1.1 Resonant zones

Figure 12a presents the acceleration-versus-drift ratio response of the structure at the southwest corner of the second story caused by a sine-sweep excitation between 0 and 2.5 Hz at DS1. The color of the curves indicates the excitation frequency. Although the force applied to the structure is proportional to the frequency, the displacement of the structure does not increase monotonically as the excitation frequency and thus the force increase. Furthermore, it can be observed that at some frequencies the structure develops hysteretic behavior, whereas at other frequencies, the displacement is not significant, despite the higher force. Figure 12b illustrates the same information along with the variation of the forcing frequency. Two resonance zones are observed: the first zone is between 1.63 to 1.70 Hz and the second zone is between 2.14 to 2.25 Hz. A range of frequencies is provided instead of specific values of the resonant frequency because the sine-sweep excitations did not allow the development of the steady-state response.

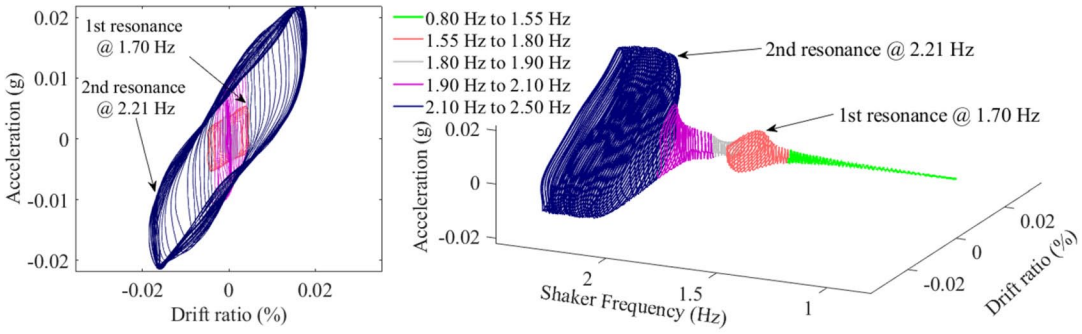

(a) Acceleration-vs.-drift ratio

(b) Acceleration-vs.-drift ratio-vs.-forcing frequency

Figure 12 Response of the structure to a sine-sweep excitation along the Y direction recorded at the southwest corner of the second story along the Y direction

Hence, the peaks of the acceleration response at different locations occur at slightly different frequencies.

The hysteretic behavior observed at the two resonant frequencies, initiates when the forced vibrations activate the existing cracks allowing the relative motion between the two sides of the cracks. Because the shaker force is proportional to its operating frequency, the shaker force applied to the building for excitation frequencies between 1.7 to 2.1 Hz is higher than the force applied during the first resonance zone that occurs around 1.7 Hz. However, the building does not displace noticeably under these higher forces as indicated by the lack of hysteretic behavior. As the excitation frequency gets close to the second resonance-frequency band, the plot demonstrates significant nonlinear behavior.

For both modes, the resonant frequencies are significantly lower than the frequencies identified from the ambient vibrations. This change of the resonant frequencies can have implications in the estimation of the seismic loads, which are commonly estimated assuming a constant period, and it is further investigated in the following sections.

6.1.2 Effect of excitation amplitude

As discussed in a previous section, the shaker mass was modified between the tests. When operating with the larger mass, the shaker could generate 3.4 times larger forces at every forcing frequency. The acceleration-versus-drift ratio responses during two sine-sweep excitations along the X direction at DS1 are shown in **Figure 13**. The two tests had

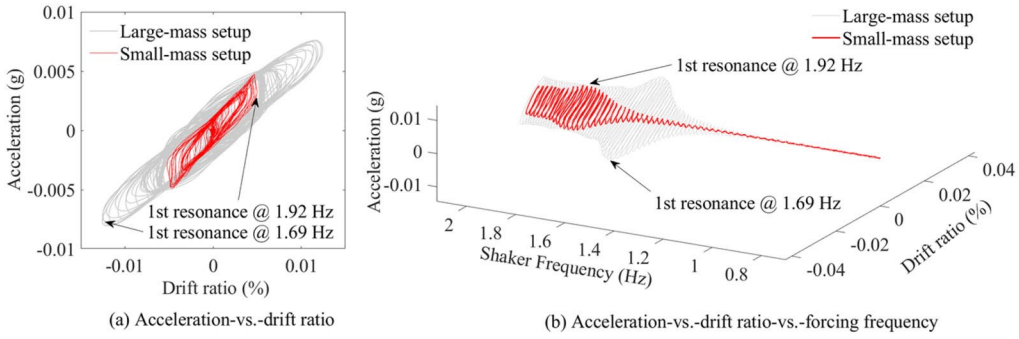

Figure 13 Response of the structure to sine-sweep excitations between 0 to 2.5 Hz along the X direction recorded at DS1 at the southwest corner of the second story along the X direction

similar forcing frequency profiles. However, the first test was performed with the small-mass setup and the second with the large-mass setup. The first resonant frequency dropped by 12% due to the increase in the amplitude of the excitation. One can also note from the plot that although resonance occurred at a lower frequency, the displacement of the structure at resonance was considerably larger when the force increased due to the larger mass. This can be justified as the increase in the shaker force led to larger motion along the cracks in the concrete and masonry elements, resulting in nonlinear behavior and the decrease of the overall stiffness of the structure. This comparison establishes a dependency between the force level and the response of the damaged structure in terms of its resonant frequency.

Sine-sweep tests with the two mass setups were also conducted along the Y direction, and the response is presented in **Figure 14**. The first and second resonant frequencies of the structure dropped by 8% and 10%, respectively, when the large-mass setup was used. The smaller frequency reductions in this loading direction can be attributed to the lack of evident damage in the infill walls on the east bays, which resisted the motion in this direction.

Figure 14 also illustrates that although the shaker mass and, subsequently, the force were increased by the factor of 3.4, the maximum acceleration on the structure increased only 1.6 times in the first resonant frequency, and 2.3 times in the case of the second resonant frequency. This lack of proportionality is another indication of the nonlinear response of the structure.

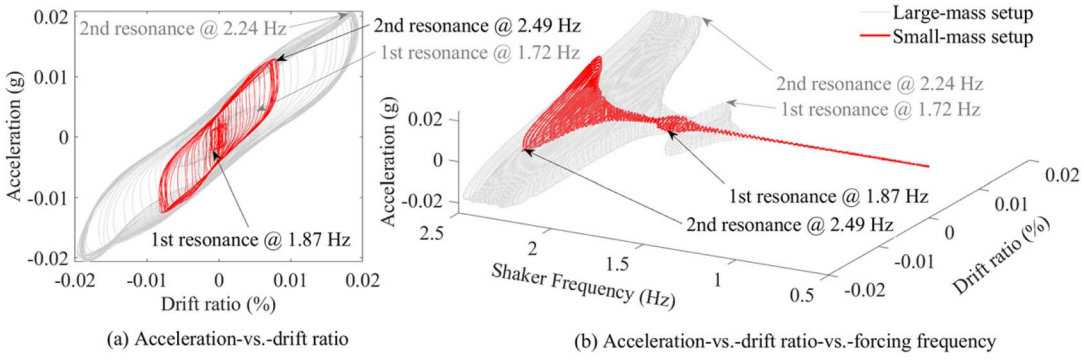

(a) Acceleration-vs.-drift ratio

(b) Acceleration-vs.-drift ratio-vs.-forcing frequency

Figure 14 Response of the structure to sine sweep excitations between 0 to 2.5 Hz along the Y direction recorded at DS1 at the northwest corner of the second story along the Y direction

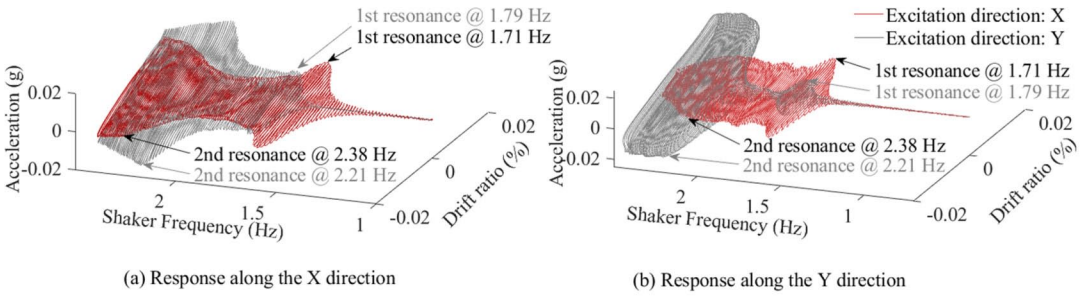

Figure 15 Response of structure to excitations along the X and Y directions recorded at the southwest corner

6.1.3 Effect of excitation direction

The forced vibrations in the X and Y directions, shown in Figures 13 and 14, indicate different frequency drops due to different excitation directions. To further investigate the effect of the excitation direction, the response of the structure during sine-sweep excitations in the X and Y directions is compared in **Figure 15**. Both tests were conducted in DS1, used the large-mass setup, and swept the frequencies between 0 and 2.5 Hz at DS1. The recorded responses along both horizontal directions indicate that the first resonant frequency under excitation along the X direction was 5% lower than that under excitation along the Y direction. The opposite trend can be observed in the second resonant zone where the resonant frequency under excitation in the Y direction was 7% lower than the resonant frequency under excitation in the X direction. Also, at both resonant zones, higher accelerations and deformations were recorded for the excitation cases that resulted in lower resonant frequencies. Considering the dependence of the shaker force on the frequency, this finding would be counterintuitive in case of linear response, as a lower excitation frequency corresponds to a lower induced force.

At the first resonant frequency, the maximum drift ratio measured along X was 53% higher when the excitation direction was along X compared to the peak drift ratio caused by excitation along Y. At the second resonant frequency, the maximum drift ratio measured along X was 35% higher when the building was excited along Y compared to excitation along X. A similar observation can be made if the response along Y is considered: the excitation along X resulted in larger deformations than the excitation along Y in the case of the first resonant frequency

and smaller deformations in the case of the second resonant frequency. These observations indicate that when the excitation was along the dominant direction of a mode, resonance of that mode occurred at a lower frequency, and resulted in larger deformations and reduced stiffness in both directions.

6.1.4 Effect of induced damage

The response of the structure to two sine-sweep excitations, performed at DS1 and DS2, between 0 to 3.0 Hz is shown in **Figure 16**a. The tests were performed before and after the removal of the infill in bay D-E/6. As indicated in the Figure, the first and second resonant frequencies dropped by 3.6% and 4.3%, respectively, during the test in DS2. A drop in resonant frequencies can be expected due to the stiffness reduction caused by the infill removal and the additional damage induced by the shaker excitations during three tests that occurred between the two tests considered here. However, the frequency drop corresponding to each source cannot be identified from this comparison.

To further investigate this, the response of the structure to two consecutive sine-sweep excitations between 0 and 5.5 Hz at DS4, shown in Figure 16b, is considered. The first and second resonant frequencies dropped by 1.8% and 2.2% between the two forced vibrations, respectively, indicating that measurable damage was induced by the forced vibrations. These values are 50% of the frequency drops observed in Figure 15a. Hence, the wall demolition and the dynamic tests have similar contributions to the induced damage. The decreasing trend of the modal frequencies at each damage state, which is estimated from the

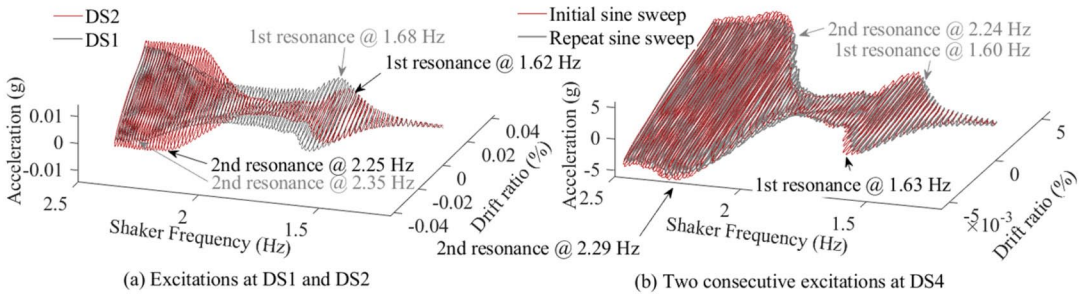

Figure 16 Comparison of the response of the structure under sine sweep excitations along the X direction recorded at the southwest corner of the second story along the X direction

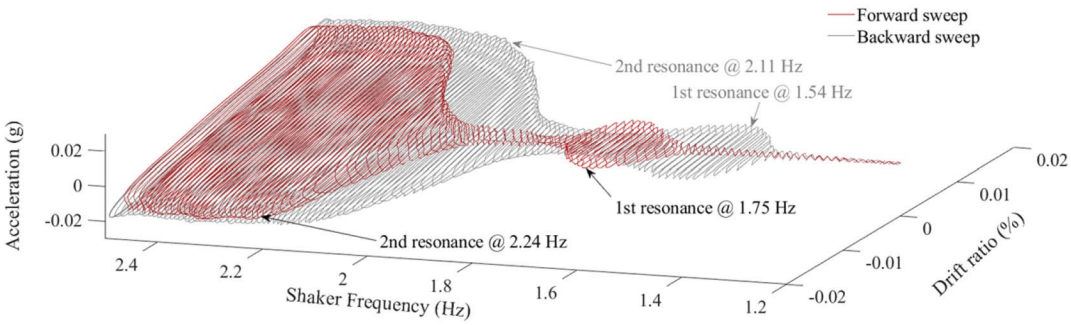

Figure 17 Structure response to a forced vibration measured along the Y direction at the southwest corner

ambient-vibration measurements after each test and shown in Figure 11, also confirms that the masonry panel removal and the dynamic tests caused comparable stiffness reduction as indicated by the nearly constant slope between DS2 and DS4.

6.1.5 Effect of initial conditions

The response of the second story during a sine-sweep excitation from 0 to 2.5 Hz is shown in **Figure 17**. The Figure includes both the branch of increasing frequencies (forward sweep), as well as the branch of decreasing frequencies (backward sweep). During the decreasing frequency branch, the first resonance occurs at a 13.6% lower frequency, while the second resonant frequency drops by 6%. Considering that the effect of the damage induced by the shaker was observed to be around 2% as discussed in the previous section, this drastic frequency reduction within the same test is mainly caused by the different initial conditions between the forward and the backward sweeps.

6.2 Steady-state response

The steady-state response of the structure was obtained from the sine-step excitations. These focused on the identified resonant frequencies and allowed the structure to vibrate under harmonic excitations with constant frequency for approximately 15 sec. Given the small frequency increment of 0.1 Hz, the structure reached its steady-state response at each target frequency after approximately 2 sec of the shaker operation at that frequency.

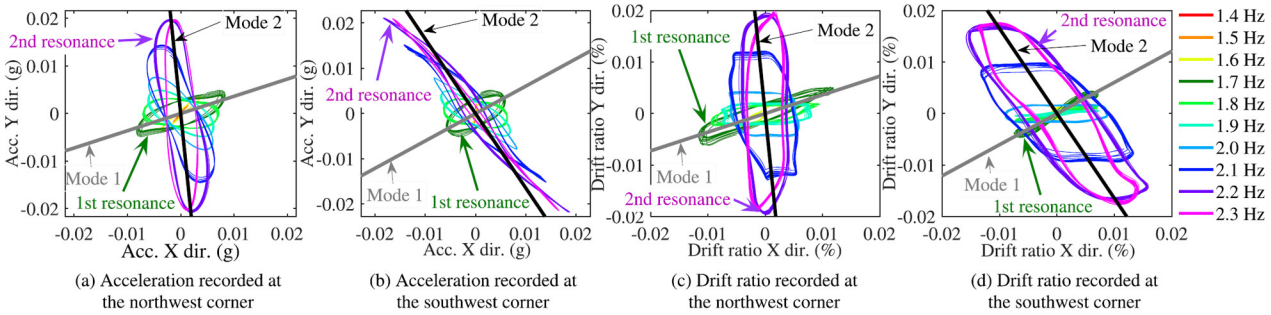

(a) Acceleration recorded at the northwest corner

(b) Acceleration recorded at the southwest corner

(c) Drift ratio recorded at the northwest corner

(d) Drift ratio recorded at the southwest corner

Figure 18 Configuration plots during a sine-step excitation along the Y direction at DS1 on the roof

The horizontal acceleration and deformation responses of the structure, referred to as configuration plots, under a sine-step excitation between 1.4 to 2.3 Hz with increments of 0.1 Hz in the Y direction at DS1 are presented in **Figures 18a & b** for two corners of the roof. Each color presents the steady-state acceleration response of the structure at a specific excitation frequency. The modal lines obtained from the ambient-vibration data using the NExT-ERA method are also shown in the Figure. The modal lines do not have the same orientation in all corners indicating torsional response. The configuration plots resemble ellipses and not straight lines due to modal interactions, the orientation of the induced force, and the nonlinearity of the structure. The orientation of each ellipse changes as the excitation frequency changes and the modal contribution to the structural response changes. The cycles corresponding to forcing frequencies of 1.7 and 2.2 Hz have axes coinciding with the modal lines. This indicates that these frequencies are closer to the resonant frequencies of the building, although they are drastically lower than the modal frequencies identified from the ambient-vibration data. The same observations can be made if the steady-state acceleration or drift-ratio response at the other corners is considered, as shown in Figures 18c and d for the drift ratios at the northwest and southwest corners.

The operational deformed shapes are compared with the corresponding mode shapes identified from the ambient-vibration measurements in Figure 8 and Table 10. The comparison indicates a good agreement with a minimum MAC value of 0.96, as reported in Table 10. However, the resonant frequencies identified during the forced vibrations, reported in Table 10, are significantly lower compared with those estimated from the

ambient-vibration recordings. For instance, at DS1, the drop is 23% for Mode 1 and 34% for Mode 2, respectively. This difference in the modal frequencies is consistently observed at all damage states, for both modes, as illustrated in Figure 11. The reduction in the natural frequency due to an increase in the amplitude of the excitation is expected as the higher forces result in the activation of more cracks and larger motion along the cracks, which increase the flexibility and period of the structure.

The effect of the excitation amplitude can also be observed from the modal frequencies estimated from the recordings during the infill-demolition process as shown in Figure 11. The equipment used for the wall demolition impacted the structure imposing impulse excitations with higher amplitudes than those of the ambient vibrations, and resulted in lower frequencies for both modes. A similar frequency drop was also observed in the dynamic response of another structure.[13] However, the drop is more significant in the case of this building due to its deterioration.

6.2.1 Effect of excitation direction

The excitation direction also affected the identified frequencies as shown in Figure 11. The resonant frequencies of the first mode during the excitations along the X direction were, in general, lower than those measured during the excitations along the Y direction at the same damage state and when the same mass was used. This can also be observed from the transient response of the structure shown in Figure 15. The first mode of the structure involved translation in the X direction and an excitation along that direction transferred more energy to the structure compared with an excitation in the Y direction. This resulted in a drop in the natural frequency as discussed in a previous section.

The steady-state response of the building recorded at two corners of the roof due to a sine-step excitation between 1.4 and 2.3 Hz in the X direction at DS1 is presented in **Figures 19a & b**. The major axis of the ellipse-shaped response during the first resonant frequency at 1.6 Hz has a similar slope as the first modal line. However, at the second resonant frequency, identified at 2.2 Hz, the shape of the plot is between an ellipse and a parallelogram. The long axis of this shape, although not precisely aligned, is close to the second modal line. It is interesting to note the change of the orientation of the main axis of the ellipse

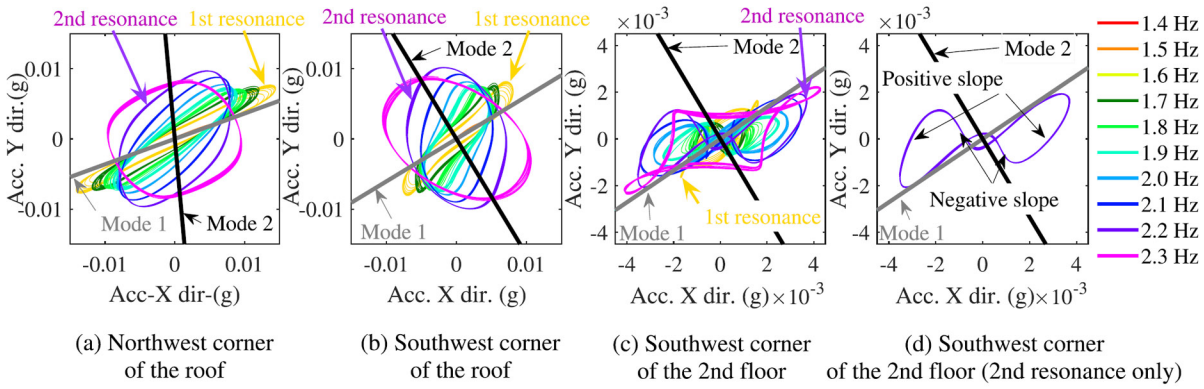

(a) Northwest corner of the roof

(b) Southwest corner of the roof

(c) Southwest corner of the 2nd floor

(d) Southwest corner of the 2nd floor (2nd resonance only)

Figure 19 Acceleration configuration plots during a sine-step excitation in the X direction at DS0

as the excitation frequency changes. The structure tends to oscillate according to its mode shapes once the excitation frequency coincides with its natural frequencies regardless of the alignment between the excitation direction and the dominant translational components of the mode. In between the resonant frequencies, the steady-state response of the structure is a combination of the two modes. It is also influenced by the point of application and direction of the excitation force, which favors Mode 1 and not Mode 2.

The change of the slope of the response is also evident in the steady-state response of the second-floor slab, shown in Figures 19c and d. In this case, the shaker was acting on the slab on which the accelerations are recorded; hence, there was a strong interaction between the structural deformations and the forces induced by the shaker. Because the shaker was acting along X, that is, the first-mode direction, the axis of the ellipse and the modal line were aligned during the first resonant frequency. However, in the second resonant frequency, the mismatch between the loading direction and the dominant translation direction of the mode resulted in negative slopes in the configuration plots. In between the two resonant frequencies, the configuration plots change due to the frequency change, but the envelope does not change as drastically as in the case of the roof slab, due to the dominance of the shaker force.

The change of the modal frequency due to the excitation direction and amplitude, discussed in a previous section, indicates that the modal properties identified using ambient-vibration recordings may not represent the dynamic properties of structures under seismic loads due to

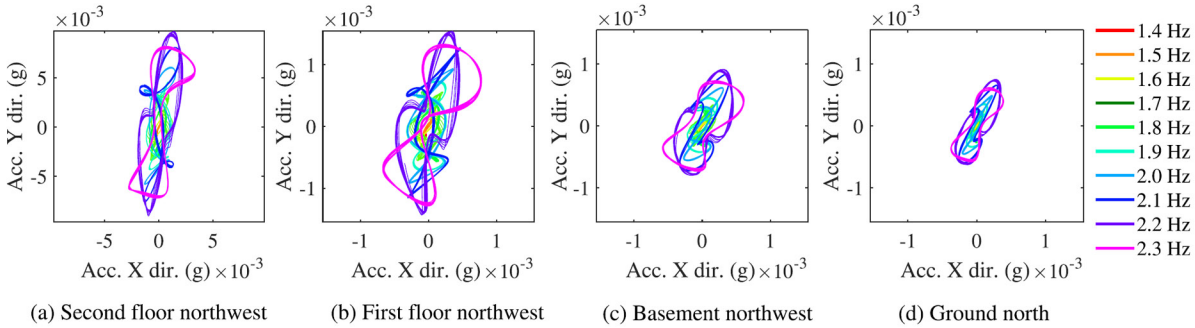

Figure 20 Acceleration configuration plots during a sine step excitation in the Y direction at DS1

nonlinearities. Hence, the effect of excitation amplitude, frequency content, and direction of the potential excitation should also be considered in the seismic assessment and design of structures.

6.3 Propagation of the motion in all stories

The steady-state response of the structure at the bottom three levels and the ground to a sine-step excitation along the Y direction between 1.4 and 2.3 Hz is illustrated in **Figure 20**. The motion at the same corner in the roof during this test is shown in Figure 18a. That Figure indicates motion amplification by roughly 100% when compared with the acceleration recorded at the shaker level shown in Figure 20a. On the contrary, the motion attenuated by approximately 86% and 91% at the first-floor slab and the basement, respectively. This observation indicates that the shaker did not excite the first floor significantly, possibly due to the confinement provided by the surrounding soil. The dissipation between the first floor and the basement, though, was not as dramatic as the attenuation between the second floor and the ground floor. Besides the difference in amplitude between the different levels, it can be seen that the axes of the elliptical shapes in the second story and below are similar to one another but different to that of the roof shown in Figure 18a. This difference indicates that the structure below the shaker can be described as rigid.

Figure 20d presents the accelerations recorded at the ground level outside the north side of the structure. It is evident that the motion recorded in the ground had similar characteristics to that recorded in the basement, but 20% lower amplitude. This indicates that there was little

dissipation between the basement and the ground as a significant portion of the energy the shaker introduced to the building was transferred to the ground and radiated away from the structure.

6.4 Lidar measurements

The collected LIDAR data were used to investigate the evolution of damage due to the forced-vibration tests in a two-step analysis process, namely surface defect detection and quantification of detected defects.[30,31] The damage features on the RC columns and masonry infills of the west side of the second story are summarized in **Tables 11 & 12**, respectively. This side was the mostly damaged side of the structure, as well as the side with better access to obtain the scans. In the case of the columns, the average width of each defect prior to and after the dynamic tests is reported. Due to the limitations of the scan resolutions, the cracks with an average width of at least 2 cm (0.8 in) are reported. For the infills, the ratio of the area of cracks in mortar joints and bricks, to the total infill area is presented. The width of the detected cracks in the columns increased with the additional width being between 0.6 and 8.7 cm (0.24 to 3.4 in). Similarly, the damage in the infills increased by between 2% to 16% of the infill area. These observations are expected and consistent with the other indications of the shaker-induced damage discussed before.

Table 11 Quantified damage in the columns on the west side of the second story

Column ID	Defect type[a]	Defect width	
		Before the tests (DS0) cm (in)	After the tests (DS4) cm (in)
A6	C	6.3 (2.5)	6.9 (2.7)
C6	S	12.4 (4.9)	13.2 (5.2)
	S	5.9 (2.3)	7.6 (3.0)
F6	C	3.8 (1.5)	4.8 (1.6)
D6	S	19.5 (7.7)	24.8 (9.8)
	CS	4.5 (1.8)	13.2 (5.2)
E6	S	5.8 (2.3)	9.3 (3.7)
	CS	5.8 (2.3)	13.6 (5.4)

a. C: cracking, S: spalling, and CS: cracking transforming to spalling.

Table 12 Damaged surface area of the infill before and after the tests (% of the total infill area)

Infill ID	A-B/6	B-C/6	C-D/6	D-E/6	E-F/6	A/2-3	A/4-5	A/5-6	G/2-3	G/3-4	G/5-6
DS0	9	15	9	23	11	9	22	12	9	16	4
DS4	11	31	15	NA[a]	NA[a]	11	24	20	11	21	NA[a]

a. Removed during the tests.

The deformation profile of the building and was also measured prior to and after the tests using the data obtained from the LIDAR scans. As discussed in a previous section, the measurement errors are estimated to be approximately one millimeter (0.04 in). Therefore, only deformations larger than the error are considered reliable. **Figure 21** illustrates the deformation profiles obtained at the corners of the structure. The profiles are shown for both the X and Y directions except for the southeast corner and the X direction at the northeast corner since no posttest data were obtained at these locations. From the plots, it is evident that the profiles are not smooth, probably due to surface roughness. Hence, they are not as informative for this level of structural deformations. However, the residual interstory drift ratio due to the tests is estimated for each floor level and reported in **Table 13**. The additional residual deformations at the northwest, southwest, and northeast corners were moderate, with maximum values of the induced interstory drift of 0.23%, 0.03%, and 0.22%, respectively, in the Y direction. The additional residual deformations in the X direction of the northwest and southwest corners

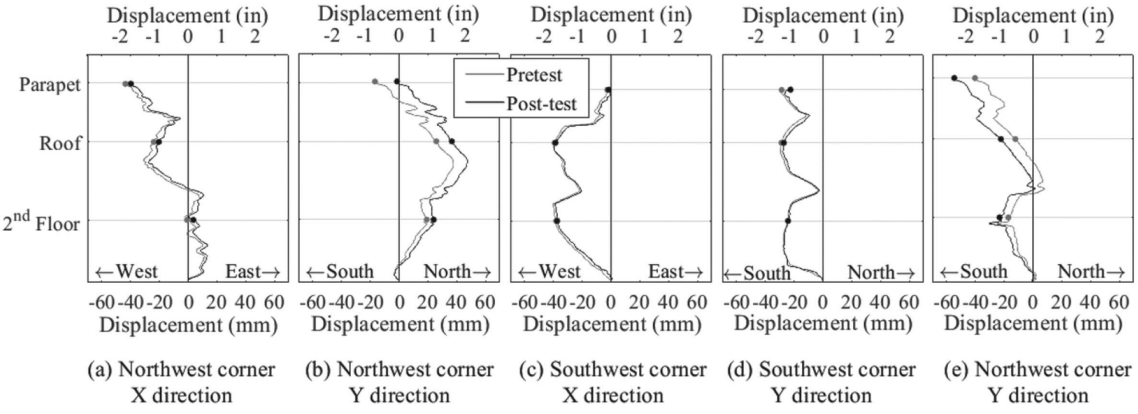

Figure 21 Pretest (DS1) and posttest (DS4) deformation profiles (the positive directions are defined as north (Y+) and east (X+), respectively)

Table 13 Computed drift/residual deformation after the test

Location	Pretest drift ratio (%)					Posttest drift ratio (%)					Residual drift ratio (%)				
	NW		SW		NE	NW		SW		NE	NW		SW		NE
	X	Y	X	Y	Y	X	Y	X	Y	Y	X	Y	X	Y	Y
Second floor	0.15	0.42	0.84	0.53	0.38	0.15	0.52	0.82	0.53	0.51	0.00	−0.10	0.02	0.00	−0.13
Roof	−0.47	0.57	0.86	0.63	0.27	−0.45	0.80	0.85	0.60	0.49	−0.02	−0.23	0.01	0.0	−0.22

were smaller. The larger additional deformations along Y can be attributed to the removal of infills along the west side, which weakened the resistance of the structure to the shaker excitations in the Y direction.

7 Conclusions

This paper discusses the dynamic response of a damaged two-story infilled RC building to harmonic excitations imposed by an eccentric-mass shaker installed inside the building. The structure, built in the 1920s, was damaged prior to the tests due to the seismic activity in the area. Additional damage was introduced during the testing sequence in four stages to investigate the effect of damage on the structural response to dynamic loads.

During the forced-vibration tests, the building exhibited significant nonlinear behavior, mainly in the second story, as the first story had been retrofitted in the 1980s. The nonlinearity caused by the damage in the columns and infills intensified when the building resonated with the induced excitation. Torsional behavior was observed in the mode shapes prior to the tests, as well as in the structural response to the forced vibrations. This was caused by the unsymmetric configurations and different damage levels in the second story infills. The damage induced in the infills during the testing sequence increased the torsional components of the response and reduced the modal frequencies. The removal of two walls in the west side (i.e., two out of the 12 walls resisting the motion along Y) resulted in 10% reduction of the second modal frequency, whereas the removal of one wall in the north side (i.e., one out of nine walls resisting motion in the X direction) reduced the first modal frequency by 5%. These observations provide experimental evidence confirming the contribution of the infills to the lateral resistance

of these structures, despite the fact that the infills were ignored in the design. This also contradicts the common assumption that the infills are nonstructural elements.

The data from the tests indicate that the range of damping values increased from 2% to 3%, measured during ambient vibrations, up to 6% to 8%, measured during forced vibrations, despite the relatively low excitation amplitude. Moreover, the resonant frequencies of the damaged structure decreased drastically, up to 34%, for the excitations induced by the shaker, when compared with the modal frequencies identified from the ambient vibrations. Frequency change up to 12% was also observed between forced vibrations with different excitation amplitudes. More considerable drop can be expected under stronger excitations caused by earthquakes. Despite the change in the frequencies, the configuration plots of the structure during resonance indicate that under the forced vibrations, the structure tended to move according to the mode shapes estimated from the ambient-vibration recordings. Moreover, the analysis of the test data demonstrates that besides the excitation amplitude, the direction also affected the resonant frequencies of the structure. Forced vibrations in the direction of a specific mode resulted in structural resonance at frequencies up to 7% lower than those resulted from forced vibrations perpendicular to that mode. Furthermore, the loading sequence within a dynamic test, or in the case of an earthquake the sequence of loading cycles, also affected the resonant frequencies and the nonlinear response of a deteriorating structure. During one test, the first resonant frequency changed by 13.6% when the initial conditions changed, although the loading amplitude and frequency were the same. These observations highlight the effects of the structural deterioration and excitation characteristics on the system-level dynamic behavior of structures, which are not well-understood, and can be consequently overlooked in practice. It is recommended that when estimating the performance of infilled RC buildings, the potential damage in the infills should be accounted for. This can be achieved using sophisticated numerical analysis tools, which can represent the evolution of damage.

Acknowledgments The study is part of a project supported by the National Science Foundation (Grant 1430180). The LIDAR processing was supported by the University of Nebraska Foundation via a Layman Seed Grant. The collaboration of NEES@UCLA during the planning and execution stages of the experiments is acknowledged. The authors also want to thank the SEES Laboratory at the University at Buffalo and the Structural Engineering Powell Laboratory of UC San Diego for testing the steel, concrete, and masonry specimens extracted from the structure, as well as Atkinson-Nolan and Associates for the in situ tests. The opinions, findings, and conclusions or recommendations discussed in this paper are those of the authors and do not necessarily represent those of the sponsors or the collaborators.

Funding National Science Foundation, Grant/ Award Number: 1430180

References

1. Al-Chaar G, Issa M, Sweeney S. Behavior of masonry-infilled nonductile reinforced concrete frames. *J Struct Eng*. 2002;128(8):1055-1063.
2. Angel R, Abrams DP, Shapiro D, Uzarski J, Webster M. Behavior of reinforced concrete frames with masonry infills. *Report No.*, 1994.
3. Crisafulli FJ. *Seismic Behaviour of Reinforced Concrete Structures with Masonry Infills*. Doctoral Dissertation. Christchurch, New Zealand: University of Canterbury; 1997.
4. Mehrabi AB, Benson Shing P, Schuller MP, Noland JL. Experimental evaluation of masonry-infilled RC frames. *J Struct Eng*. 1996;122 (3):228-237.
5. Pujol S, Fick D. The test of a full-scale three-story RC structure with masonry infill walls. *Eng Struct*. 2010;32(10):3112-3121.
6. Centeno J, Ventura C, Foo S. Shake table testing of gravity load designed reinforced concrete frames with unreinforced masonry infill walls. *Proceedings of The 14th World Conference on Earthquake Engineering, Beijing China*, 2008.
7. Hashemi A, Mosalam KM. Shake-table experiment on reinforced concrete structure containing masonry infill wall. *Earthq Eng Struct Dyn*. 2006;35(14):1827-1852.
8. Lee HS, Woo SW. Effect of masonry infills on seismic performance of a 3-storey R/C frame with non-seismic detailing. *Earthq Eng Struct Dyn*. 2002;31(2):353-378.
9. Stavridis A, Koutromanos I, Shing P. Shake-table tests of a three-story reinforced concrete frame with masonry infill walls. *Earthq Eng Struct Dyn*. 2012;41(6):1089-1108.
10. Department of Conservation. California Strong Motion Instrumentation Program (CSMIP), 2019.
11. De Sortis A, Antonacci E, Vestroni F. Dynamic identification of a masonry building using forced vibration tests. *Eng Struct*. 2005;27(2): 155-165.
12. Englekirk RE, Matthiesen R. Forced vibration of an eight-story reinforced concrete building. *Bull Seismol Soc Am*. 1967;57(3):421-436.

13. Yousefianmoghadam S, Behmanesh I, Stavridis A, Moaveni B, Nozari A, Sacco A. System identification and modeling of a dynamically tested and gradually damaged 10-story reinforced concrete building. *Earthq Eng Struct Dyn*. 2017;47(1):25-47. https://doi.org/10.1002/eqe.2935
14. American Concrete Institute. , ACI 318 14: building code requirements for structural concrete and commentary, 2014.
15. TMS 402/602 Building Code Requirements and Specification for Masonry Structures. , 2016.
16. ASTM. , *C1197-14a: Standard Test Method for In Situ Measurement of Masonry Deformability Properties Using the Flatjack Method*, West Conshohocken, PA: ASTM International; 2014. https://doi.org/10.1520/C1197-14A.
17. ASTM. , *C1196-14a: Standard Test Method for In Situ Compressive Stress Within Solid Unit Masonry Estimated Using Flatjack Measurements*, West Conshohocken, PA: ASTM International; 2014. https://doi.org/10.1520/C1196-14A.
18. ASTM. *C1531-15: Standard Test Methods for In Situ Measurement of Masonry Mortar Joint Shear Strength Index*. ASTM International: West Conshohocken, PA; 2015. https://doi.org/10.1520/C1531-15
19. David D, Dolan C, Nilson A. *Design of Concrete Structures*. 15th ed. New York: McGraw Hill; 2016.
20. Stewart JP, Whang DH, Wallace JW, Nigbor R. Field testing capabilities of nees@ UCLA equipment site for soil-structure interaction applications. *Proceedings of Earthquake engineering and soil dynamics, Proceedings of sessions of the geo-frontiers* 2005 *congress, ASCE Geotech. Special Publication*, Austin, TX, 2005.
21. ASTM. , *E2544-11a: Standard Terminology for Three-Dimensional (3D) Imaging Systems*, ASTM International, 2011, https://doi.org/10.1520/E2544-11A
22. Davies L, Gather U. The identification of multiple outliers. *J Am Stat Assoc*. 1993;88(423):782-792.
23. Yousefianmoghadam S. Investigation of the linear and non-linear dynamic behavior of existing reinforced concrete buildings through tests and simulations. Ph.D. Dissertation, State University of New York at Buffalo, 2019.
24. Welch PD. The use of fast Fourier transform for the estimation of power spectra: A method based on time averaging over short, modified periodograms. *IEEE Transactions on audio and electroacoustics*. 1967;15(2):70-73.
25. Oppenheim AV, Schafer RW, Buck JR. *Discrete-time signal processing*. Englewood Cliffs, NJ: Prentice Hall, 1989.
26. Farrar C, James IG. System identification from ambient vibration measurements on a bridge. *J Sound Vib*. 1997;205(1):1-18.
27. Juang J-N, Pappa RS. An eigensystem realization algorithm for modal parameter identification and model reduction. *J Guid Control Dynam*. 1985;8(5):620-627.
28. Bendat JS, Piersol AG. *Engineering Applications of Correlation and Spectral Analysis*. 315 New York: Wiley-Interscience; 1980.
29. Allemang RJ, Brown DL. A correlation coefficient for modal vector analysis. *Proceedings of the 1st international modal analysis conference*, 1982.

30. Bose S, Nozari A, Mohammadi M, et al. Structural assessment of a school building in Sankhu, Nepal damaged due to torsional response during the 2015 Gorkha earthquake. In: *Proceedings of IMAC XXXIV, A Conference and Exposition on Structural Dynamics*. Orlando, FL: Springer; 2016.
31. Mohammadi ME, Wood RL, Wittich CE. Non-temporal point cloud analysis for surface damage in civil structures. *ISPRS Int J Geo Inf*. 2019;8(12):527-553.